Journal of Constructional Steel Research 179 (2021) 106566

Contents lists available at ScienceDirect

Journal of Constructional Steel Research

Experimental and numerical investigations of circular recycled aggregate concrete-filled stainless steel tube columns

An He [a], Andi Su [a], Yating Liang [b], Ou Zhao [a,*]

[a] School of Civil and Environmental Engineering, Nanyang Technological University, Singapore
[b] School of Engineering, University of Glasgow, Glasgow, UK

ARTICLE INFO

Article history:
Received 10 October 2020
Received in revised form 31 January 2021
Accepted 2 February 2021
Available online 17 February 2021

Keywords:
Circular recycled aggregate concrete-filled stainless steel tube columns
Design analyses
Flexural buckling
Initial geometric imperfection measurements
Material tests
Numerical modelling
Pin-ended column tests
Recycled coarse aggregate replacement ratio

ABSTRACT

This paper reports a comprehensive experimental and numerical study of the flexural buckling behaviour and resistances of circular recycled aggregate concrete-filled stainless steel tube columns. The experimental programme, adopting four series of column specimens designed with various stainless steel tube sizes, recycled coarse aggregate replacement ratios and member lengths, included material tests on both recycled aggregate concretes and stainless steel tubes, initial global geometric imperfection measurements and pin-ended column tests. The obtained experimental results, including the failure loads, load–mid-height lateral deflection curves and flexural buckling failure modes, were reported in detail. The effects of the stainless steel tube size, recycled coarse aggregate replacement ratio and member length on the flexural buckling resistances of the column specimens were examined. The lateral deflection distributions along the column specimen lengths and the development of the longitudinal strains of the outer stainless steel tubes were discussed. The experimental programme was supplemented by a numerical modelling programme, in which finite element models were developed and validated against the test results and then used for conducting parametric studies to generate further numerical data over a wide range of cross-section dimensions and member lengths. Given that there have been no existing design codes for recycled aggregate concrete–stainless steel composite structures, the relevant codified design rules for circular natural aggregate concrete-filled carbon steel tube columns failing by flexural buckling, as used in Europe, Australia/New Zealand and America, were assessed for their applicability to circular recycled aggregate concrete-filled stainless steel tube columns, based on the test and numerical data. The assessment results revealed that the design rules, as given in the Australian/New Zealand standard and American specification, result in unsafe flexural buckling resistance predictions when used for circular recycled aggregate concrete-filled stainless steel tube columns, while the Eurocode design rules lead to more safe and accurate flexural buckling resistance predictions.

1. Introduction

The past two decades have witnessed an increasing use of sustainable construction materials in structural and bridge engineering practices. Moreover, emphases are also placed on the use of construction and demolition wastes as raw materials, in order to reduce the dependence on natural raw materials and bring down the impact of construction and demolition wastes on the environment. Recycled aggregate concrete (RAC) is a type of sustainable concrete that is produced using coarse aggregates recycled from construction and demolition wastes. Compared with nature coarse aggregates (NCA), recycled coarse aggregates (RCA) have inferior mechanical properties due to physical and chemical damages during the recycling process and thus the resulting RAC possesses lower strength, stiffness and ductility than the conventional natural aggregate concrete (NAC) [1]. Therefore, RAC is currently mainly used to fabricate non-structural (non-load bearing) components, which greatly limits the application of RAC. Given that lateral confinement is an effective way to improve the axial (longitudinal) strength and ductility of concrete and can be achieved by means of the circular concrete-filled steel tube (CFST) composite system [1], an idea of using the circular CFST composite system but infilled with RAC has been prompted, which could greatly increase the strength and ductility of RAC and thus brings the possibility of extending the application scope of RAC to general load-bearing components.

Previous studies on circular RAC-filled steel tube members were briefly summarised herein. At cross-sectional level, a series of tests were conducted on circular RAC-filled carbon steel tube stub columns [2–6] to study their compressive behaviour and resistances, while the flexural behaviour and resistances of circular RAC-filled carbon steel tube beams were investigated by Yang and Han [2] and Chen et al. [5] through bending tests. At member level, Yang and Han [7] and Chen

* Corresponding author.
E-mail address: ou.zhao@ntu.edu.sg (O. Zhao).

https://doi.org/10.1016/j.jcsr.2021.106566
0143-974X/

et al. [5] experimentally studied the flexural buckling behaviour of circular RAC-filled carbon steel tube long columns and long beam-columns, respectively, examined their resistances and quantified the reductions in resistances over the corresponding circular NAC-filled carbon steel tube members. Research was also conducted on circular RAC-filled carbon steel tube columns under extreme loading conditions. Specifically, Tang et al. [8,9] conducted lateral cyclic loading tests on circular RAC-filled carbon steel tube columns to investigate their seismic performance and deformability and verified the feasibility of using them in seismic regions. Li et al. [10] carried out compression tests on circular RAC-filled carbon steel tube stub columns after exposure to fire and quantified their post-fire residual resistances and stiffnesses. Recently, the use of stainless steels in civil and offshore engineering becomes increasingly popular, as stainless steels possess more advantageous material properties, including higher strength and ductility than carbon steels; moreover, stainless steels are sustainable, owing to the superior durability and 100% recyclable nature. In comparison with the comprehensive research on RAC-filled carbon steel tube members, investigations into RAC-filled stainless steel tube (RACFSST) members remain limited, with the only study carried out by Yang and Ma [11] on RACFSST stub columns and beams. A research programme has thus been initiated by the authors to investigate the behaviour and resistances of various types of circular RACFSST members.

This paper presents testing and numerical modelling of circular RACFSST long columns failing by flexural buckling. A testing programme, including material tests on stainless steel tubes and RAC infill as well as initial global geometric imperfection measurements and pin-ended compression tests on twelve circular RACFSST column specimens, was firstly carried out. A complementary numerical modelling programme was then conducted and involved a validation study to validate the developed finite element models against the experimental results and a parametric study to expand the test data bank on circular RACFSST columns over an extended range of cross-section dimensions and member lengths. Due to the lack of design codes for RACFSST composite structures, the relevant design rules for circular natural aggregate concrete-filled carbon steel tube columns failing by flexural buckling, as specified in EN 1994-1-1 [12], AS/NZS 5100 [13] and AISC 360 [14], were assessed for their applicability to circular RACFSST columns, based on the test and numerical data.

2. Experimental programme

2.1. Test specimens

Given that there have been no existing tests on circular RACFSST columns failing by flexural buckling, an experimental programme was firstly conducted to generate a test data bank. The experimental programme included twelve circular RACFSST column specimens fabricated with varying RCA replacement ratios (the mass percentages of NCA replaced by RCA in concrete), stainless steel tube sizes and member lengths. Specifically, two grade EN 1.4301 austenitic stainless steel circular hollow sections CHS 89 × 3 and CHS 101 × 3 were adopted, and for each circular hollow section, two nominal member lengths (700 mm and 1200 mm) were selected; this resulted in a total of four specimen series – D89-L700, D89-L1200, D101-L700 and D101-L1200. The designation system of each specimen series started with a letter 'D' (representing diameter) and the nominal outer tube diameter, followed by a letter 'L' (representing length) and the nominal member length. Each specimen series included three column specimens, with different RCA replacement ratios – 0%, 35% and 70%, i.e. one reference NAC-filled stainless steel tube (NACFSST) column specimen and two RACFSST column specimens. The column specimen ID consisted of the specimen series and the RCA replacement ratio; for example, the specimen D101-L1200-R35 represents a 1200 mm circular RACFSST column specimen fabricated from the austenitic stainless steel CHS 101 × 3 tube and recycled aggregate concrete with the RCA replacement ratio of 35%. The RCA replacement ratio r and the measured geometric sizes for each of the circular RACFSST and NACFSST column specimens, including the outer diameter D and wall thickness t of the stainless steel CHS tube as well as the member length L, are reported in Table 1.

2.2. Material tests

Single-sized RCA with a nominal size of 20 mm (one of the most commonly used RCA products), together with single-sized NCA with a nominal size of 10 mm and graded NCA with a continuous range of nominal sizes from 5 mm to 20 mm, were adopted for fabricating the required recycled and natural aggregate concretes. The physical properties of the RCA and two types of NCA, including the loose bulk density, apparent particle density and water absorption ratio, were carefully measured according to BS EN 1097–3 [15] and BS EN 1097–6 [16], as reported in Table 2. The actual particle size distribution of each type of coarse aggregates was measured by means of the sieving method given in BS EN 933–1 [17], with the grading curves displayed in Fig. 1, where the percentages passing by mass are plotted against the sieve sizes of 2.5 mm, 5 mm, 10 mm, 20 mm and 28 mm, respectively; the requirements for Grading Category $G_C80/20$, as specified in BS EN 12620 [18], are given in Table 3 and also represented as an envelope in Fig. 1. For each of the three examined types of concrete, namely R0, R35 and R70 (denoting concretes with the RCA replacement ratios of 0%, 35% and 70%, respectively), the single-sized RCA as well as the single-sized and graded NCA were mixed such that (i) the required RCA replacement ratio was achieved and (ii) the grading requirements were satisfied, with their proportions reported in Table 4 and the resulting grading curves (within the grading envelope) shown in Fig. 1. The weights of other materials used for each type of concrete are also reported in Table 4. Note that prior to concrete casting, all the RCA were firstly sun-dried and then pre-wetted through adding additional water, to compensate for the high-water absorption of the RCA from a dry state to a saturated surface dry condition and achieve the same effective water-to-cement ratio for the three types of concrete R0, R35 and R70 [1]; the required weight of the additional water was calculated based on the measured water absorption ratio of the RCA – see Table 2. For each type of concrete, four cylinder samples were reserved during the casting and then cured together with the corresponding column specimens. Concrete cylinder tests were conducted at the time of pin-ended column tests. The setup for concrete cylinder tests is shown in Fig. 2, in which two strain gauges are attached to the concrete cylinder sample to measure the compressive strains. A uniform rate equal to 0.6 MPa/s was used to perform all the concrete cylinder tests and the method specified in BS EN 12390–13 [19] was adopted to measure the concrete secant modulus. The average measured compressive strength f_c and secant modulus E_{cm} from the four concrete cylinder samples for each type of concrete are listed in Table 1.

Table 1
Measured geometric dimensions and material properties of circular RACFSST and NACFSST column specimens.

Specimen ID	r (%)	D (mm)	t (mm)	L (mm)	L_e (mm)	f_c (MPa)	E_{cm} (MPa)	ω_g (mm)
D89-L700-R0	0	88.75	2.81	701	811	67.5	34994	0.14
D89-L700-R35	35	88.68	2.84	702	812	58.5	34432	0.16
D89-L700-R70	70	88.87	2.82	701	811	52.4	31060	0.07
D89-L1200-R0	0	88.58	2.76	1202	1312	67.5	34994	0.18
D89-L1200-R35	35	88.79	2.86	1202	1312	58.5	34432	0.38
D89-L1200-R70	70	88.80	2.78	1201	1311	52.4	31060	0.30
D101-L700-R0	0	101.17	2.85	702	812	67.5	34994	0.34
D101-L700-R35	35	101.45	2.86	700	810	58.5	34432	0.10
D101-L700-R70	70	101.52	2.86	701	811	52.4	31060	0.10
D101-L1200-R0	0	101.22	2.86	1200	1310	67.5	34994	0.23
D101-L1200-R35	35	101.29	2.86	1201	1311	58.5	34432	0.69
D101-L1200-R70	70	101.41	2.85	1201	1311	52.4	31060	0.42

Table 2
Physical properties of recycled and natural coarse aggregates.

Type	Loose bulk density (g/cm^3)	Apparent particle density (g/cm^3)	Water absorption ratio (%)
5–20 mm NCA	1.46	2.63	1.00
10 mm NCA	1.47	2.71	1.40
20 mm RCA	1.24	2.62	7.18

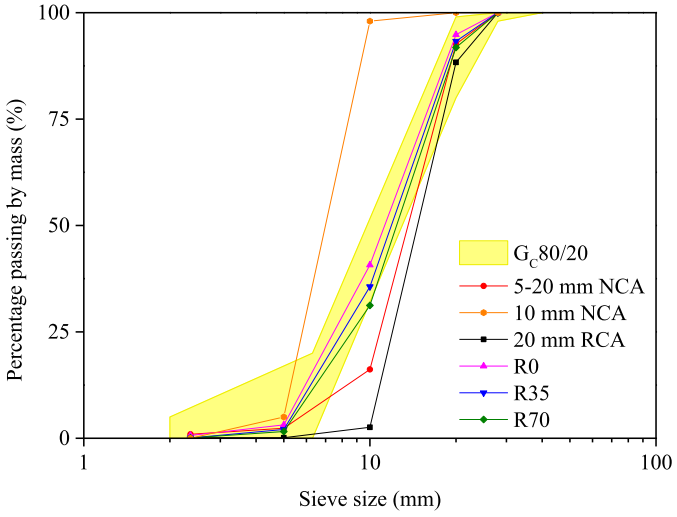

Fig. 1. Grading curves of coarse aggregates.

Table 3
Requirements for Grading Category G$_C$80/20 in BS EN 12620 [18].

Sieve size (mm)	Percentage passing by mass
40	100
28	98–100
20	80–99
6.3	0–20
2	0–5

The material properties of the austenitic stainless steel CHS tubes were measured from tensile coupon tests, with the setup displayed in Fig. 3, where the instrumentation includes an extensometer to measure the elongation within a 50 mm gauge length and a pair of strain gauges to record the strains. A two-stage displacement-controlled loading scheme was used for the tensile coupon tests. Specifically, the displacement rate was initially kept at 0.05 mm/min up to the nominal 0.2% proof stress and then increased to 0.8 mm/min. The resulting strain

Table 4
Mixture proportions of concretes.

Type	5–20 mm NCA (kg)	10 mm NCA (kg)	20 mm RCA (kg)	Sand (kg)	Cement (kg)	Water (kg)	Additional water (kg)
R0	548.9	235.2	0.0	784.1	480.0	240.0	0.0
R35	273.9	234.8	282.6	782.5	480.0	240.0	19.7
R70	0.0	234.3	564.1	781.0	480.0	240.0	39.4

Fig. 2. Concrete cylinder test setup.

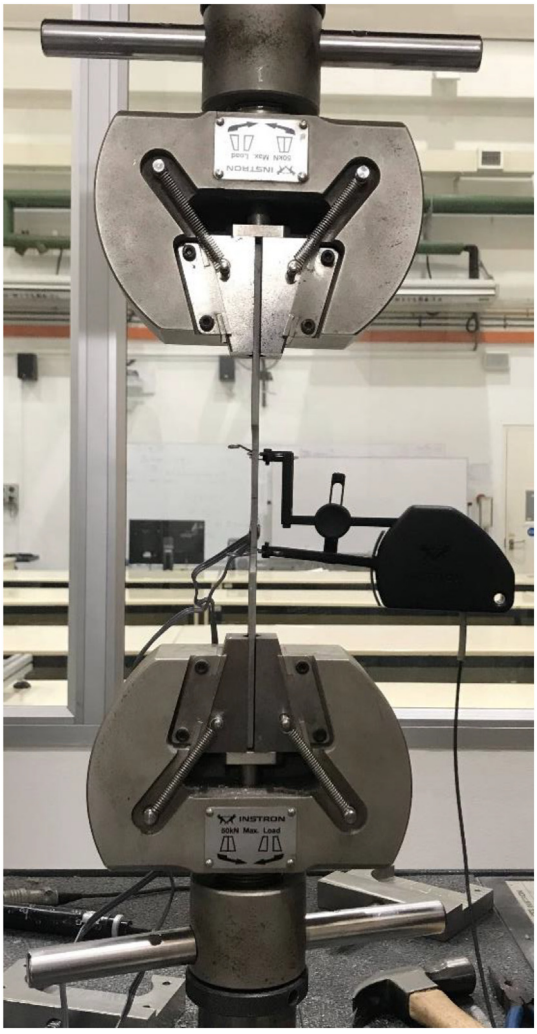

Fig. 3. Tensile coupon test setup.

rates of the parallel necked portion of each coupon satisfied the rules prescribed in EN ISO 6892-1 [20]. Fig. 4 depicts the stressstrain curves of the austenitic stainless steel CHS 89 × 3 and CHS 101 × 3. The key average material properties were then determined from the measured stress-strain curves and are reported in Table 5, in which E is the Young's modulus, $\sigma_{0.2}$ and $\varepsilon_{0.2}$ are the 0.2% proof stress and the corresponding strain at the 0.2% proof stress, σ_u and ε_u are the ultimate stress and the corresponding strain at the ultimate stress, and n and m are the coefficients used in the Ramberg-Osgood material model [21–26].

2.3. Initial global geometric imperfection measurements

The global buckling behaviour and resistances of composite columns are affected by their initial global geometric imperfections. Therefore, the initial global geometric imperfection magnitude of each circular RACFSST or NACFSST column specimen was measured. The test setup for initial global geometric imperfection measurements is shown in Fig. 5, where a column specimen is mounted on the work bench of a CNC router and a LVDT is moved along the uppermost edge line of the column specimen, with the readings respectively recorded near the two ends and at mid-height. The initial mid-height global geometric imperfection magnitude of the column specimen in the radial direction was then given as the deviation from a linear reference line (i.e. a linear line connecting the data points measured at the two ends) to the measured data point at mid-height. The column specimen was then rotated at an interval of 60 degrees, with the measurement procedures repeated, to obtain the initial mid-height global geometric imperfection magnitudes in another five radial directions – see Fig. 5. The final value of the initial mid-height global geometric imperfection of each column specimen ω_g was defined as the maximum magnitude measured in all the six radial directions, as reported in Table 1.

2.4. Pin-ended column tests

Compression tests were conducted on twelve circular RACFSST and NACFSST column specimens to investigate their flexural buckling behaviour and resistances. Surface treatments of the top and bottom ends of each column specimen, including milling the ends and covering the ends with high strength gypsum, were performed before testing, to

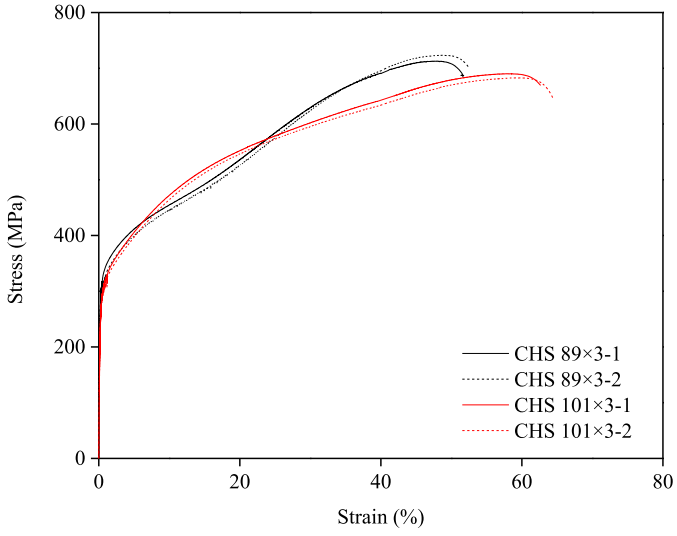

Fig. 4. Stress–strain curves of stainless steel CHS tubes.

Table 5
Measured key average material properties of stainless steel CHS tubes.

Cross-section	E (GPa)	$\sigma_{0.2}$ (MPa)	$\varepsilon_{0.2}$ (%)	σ_u (MPa)	ε_u (%)	n	m
CHS 89 × 3	198	303.9	0.353	712.9	48.0	4.0	2.5
CHS 101 × 3	197	271.8	0.340	690.2	55.4	3.3	2.4

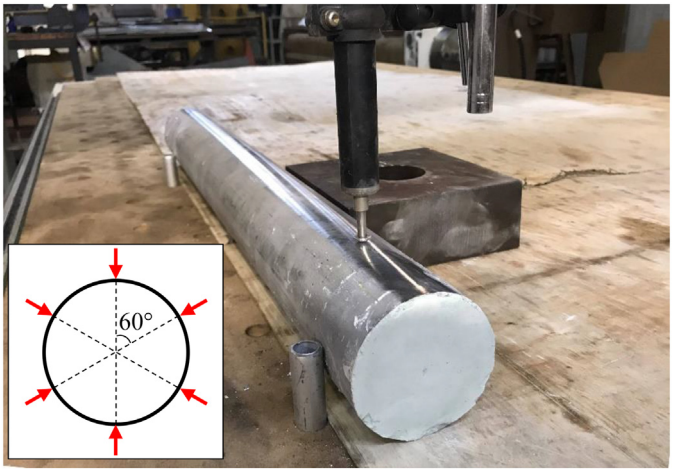

Fig. 5. Test setup for initial global geometric imperfection measurements.

ensure that the end surfaces of each column specimen were flat and parallel. An Instron 5000 kN servo-hydraulic testing machine was used to apply compression loads onto the column specimens, with a uniform displacement rate of 0.3 mm/min. Both ends of the testing machine were equipped with knife-edge devices, as shown in Fig. 6, in order to provide pin-ended boundary conditions to the ends of the column specimens. Each knife-edge device consisted of a pit plate containing a semi-circular groove and a wedge plate with a knife-edge wedge. Prior to testing, a column specimen was positioned between the top and bottom knife-edge devices and oriented such that the radial direction leading to the maximum initial mid-height global geometric imperfection magnitude was perpendicular to the knife-edges. Note that the distance from the rotation centre of the knife-edge device to the end of the column specimen is equal to 55 mm (see Fig. 6); therefore, the effective length of each column specimen L_e is equal to $L + 110$ mm, as reported in Table 1.

The instrumentation adopted for the pin-ended column tests is depicted in Fig. 6, including (i) a LVDT vertically installed at the top rigid platen of the testing machine to measure the end shortening of the column specimen, (ii) three LVDTs horizontally positioned at distances of 0.25 L, 0.5 L and 0.75 L from the bottom end of the column specimen to record the lateral deflections along the buckling direction at these three positions and thus capture the lateral deflection distribution pattern along the column length, and (iii) three strain gauges, respectively attached to the two extreme fibres (#1 and #3 - see Fig. 6) and the mid-point of the extreme fibres (#2 - see Fig. 6) of the stainless

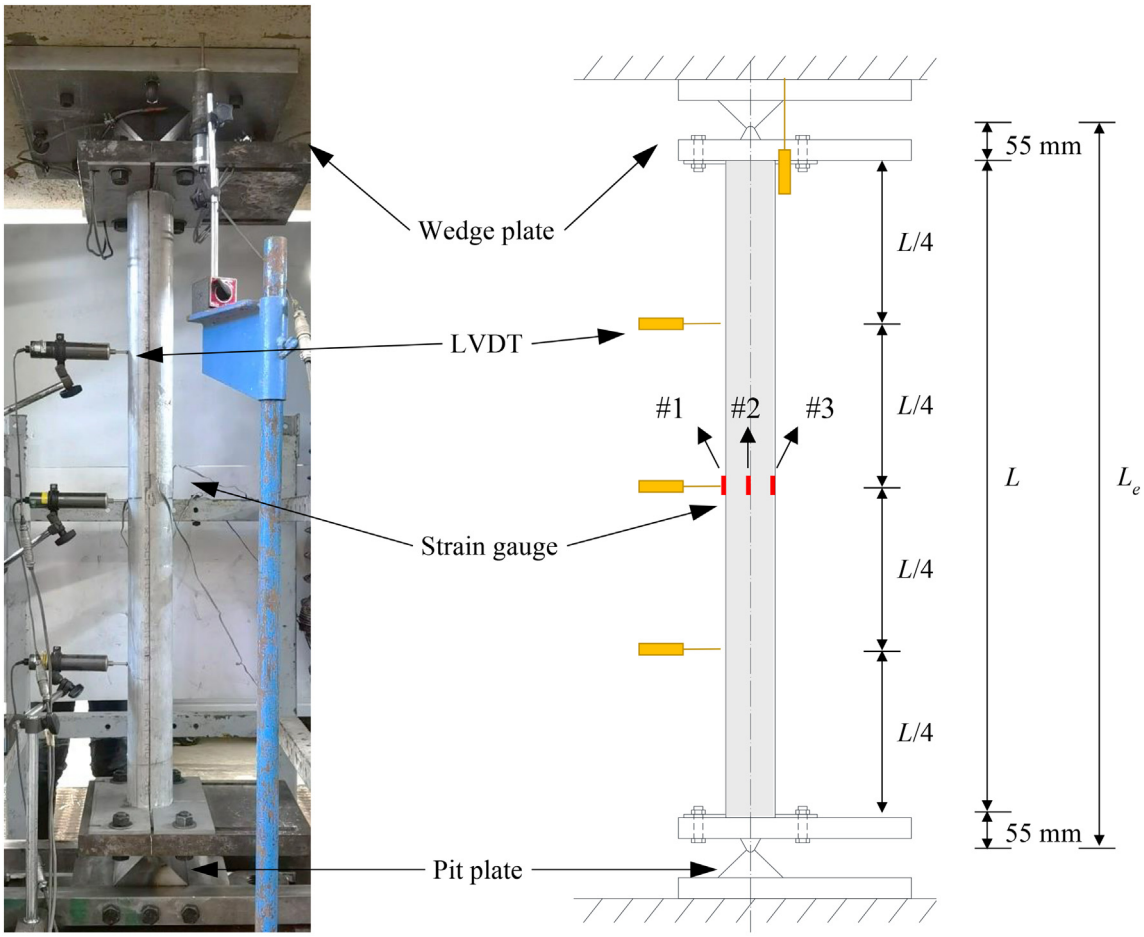

Fig. 6. Pin-ended column test setup.

steel tube at mid-height, to obtain the longitudinal strains at these three positions. The mid-height lateral deflection, as recorded by the LVDT, and the longitudinal strains of the two extreme fibres, as measured from the strain gauges #1 and #3, were then adopted to calculate the actual value of the overall global geometric imperfection, defined as the summation of the initial mid-height global geometric imperfection magnitude ω_g and the initial loading eccentricity e_0, for each column specimen, based on Eq. (1) [27–29], where N is the applied compression load, ε_{max}-ε_{min} is the difference of the longitudinal strains of the two extreme fibres, Δ is the mid-height lateral deflection and $(EI)_h = E_{cm}I_c + EI$ is the flexural stiffness, in which I_c and I are the second moments of area of the inner concrete and outer stainless steel tube, respectively. Note that Eq. (1) was derived based on the assumption that the structural behaviour was close to linear elastic and therefore a small alignment load approximately equal to 10% of the expected failure load was applied onto each column specimen for calculating the overall global geometric imperfection magnitude $(\omega_g + e_0)$ [27–29]. If the calculated $(\omega_g + e_0)$ was greater than L_e/1000, the position of the column specimen was carefully re-adjusted until the achievement of $(\omega_g + e_0) < L_e$/1000 [27–29]. Table 6 reports the final overall global geometric imperfection magnitude for each column specimen, with the largest normalised value $(\omega_g + e_0)/L_e$ equal to 1/1192. Moreover, the member relative slenderness of each column specimen $\overline{\lambda}_{EC4}$, as specified in EN 1994-1-1 [12], was calculated from Eq. (2), where $N_{pl,Rk} = A_c f_c + A_s \sigma_{0.2}$ is the summation of the plastic resistances of the concrete infill and stainless steel tube and N_{cr} is the elastic critical normal force and given by Eq. (3), where $(EI)_{eff,EC4}$ is the EC4 effective flexural stiffness and defined by Eq. (4), and also reported in Table 6.

$$\omega_g + e_0 = \frac{(EI)_h(\varepsilon_{max} - \varepsilon_{min})}{DN} - \Delta \tag{1}$$

$$\overline{\lambda}_{EC4} = \sqrt{\frac{N_{pl,Rk}}{N_{cr}}} \tag{2}$$

$$N_{cr} = \frac{\pi^2 (EI)_{eff,EC4}}{L_e^2} \tag{3}$$

$$(EI)_{eff,EC4} = EI + 0.6E_{cm}I_c \tag{4}$$

All the twelve circular RACFSST and NACFSST column specimens underwent noticeable global deformations upon testing and failed by member flexural buckling, with the deformed failure modes from a typical specimen series D89-L1200 displayed in Fig. 7. The measured load–mid-height lateral deflection curves of the four series of circular RACFSST and NACFSST column specimens are shown in Figs. 8(a)–8(d), respectively. Table 6 presents the key obtained test results, including the failure load N_u, the mid-height lateral deflection at the failure load Δ_u and the reduction factor for flexural buckling χ, as given by Eq. (5), in which A_c and A_s are the cross-section areas of the concrete infill and stainless steel tube, respectively.

$$\chi = \frac{N_u}{f_c A_c + \sigma_{0.2} A_s} \tag{5}$$

Table 6
Key experimental results of circular RACFSST and NACFSST column specimens.

Specimen ID	$\omega_g + e_0$ (mm)	$\overline{\lambda}_{EC4}$	N_u (kN)	Δ_u (mm)	χ
D89-L700-R0	0.66	0.46	525	3.21	0.88
D89-L700-R35	0.56	0.44	504	3.52	0.92
D89-L700-R70	0.68	0.43	481	4.11	0.93
D89-L1200-R0	0.51	0.75	498	3.38	0.84
D89-L1200-R35	0.26	0.71	429	3.68	0.78
D89-L1200-R70	0.63	0.70	424	3.12	0.83
D101-L700-R0	0.14	0.40	737	1.67	1.02
D101-L700-R35	0.28	0.38	670	2.69	1.01
D101-L700-R70	0.34	0.38	639	2.49	1.03
D101-L1200-R0	1.00	0.65	575	4.86	0.79
D101-L1200-R35	1.10	0.62	555	4.90	0.84
D101-L1200-R70	1.09	0.61	540	5.29	0.88

2.5. Discussion on test results

2.5.1. Lateral deflection

The lateral deflection distributions along the member lengths of the circular RACFSST and NACFSST column specimens, together with the mid-height lateral deflections at the failure loads, are discussed in this section. Figs. 9(a)–9(c) depict the lateral deflections of a typical NACFSST column specimen D89-L700-R0 and two typical RACFSST column specimens D89-L700-R35 and D89-L700-R70 (i.e. from the specimen series D89-L700), measured by the three horizontal LVDTs at five specific load levels of $0.5N_u$, $0.7N_u$, $0.8N_u$, $0.9N_u$ and N_u. It was found that (i) the lateral deflections of both the NACFSST and RACFSST column specimens were not obvious when the applied compression loads were less than $0.5N_u$, (ii) the lateral deflections of both the NACFSST and RACFSST column specimens increased gradually as the applied compression loads increased from $0.5N_u$ to $0.9N_u$, after which a rapid growth of the lateral deflections was observed near the failure load N_u, and (iii) the overall lateral deflection distribution patterns along the member lengths of both the NACFSST and RACFSST column specimens are approximate of half-sine wave shapes. The measured mid-height lateral deflections at the failure loads, as reported in Table 6, were generally shown to increase with the member lengths. For example, the mid-height lateral deflections for the two typical RACFSST column specimens D101-L700-R70 and D101-L1200-R70 (with the same stainless steel CHS size and RCA replacement ratio but different member lengths) are respectively equal to 2.49 mm and 5.29 mm at the failure loads; this is because longer columns are more susceptible to flexural buckling, with larger global deformations. Moreover, for each specimen series, the columns with higher RCA replacement ratios generally exhibited larger mid-height lateral deflections at failure, owing to the lower member flexural stiffnesses $(EI)_h = E_{cm}I_c + EI$ (E_{cm} is smaller for RAC with higher RCA replacement ratio) and higher susceptibility to flexural buckling.

2.5.2. Flexural buckling resistance

The effects of the stainless steel tube size, RCA replacement ratio and member effective length on the flexural buckling resistances of the circular RACFSST column specimens are discussed herein. The failure loads of each series of the column specimens are plotted in the histograms and displayed in Figs. 10(a) and 10(b), where a clear decreasing trend of the failure loads is demonstrated for each specimen series as the RCA replacement ratios increase. For example, the failure loads of the RACFSST column specimens D89-L1200-R35 (with the RCA replacement ratio equal to 35%) and D89-L1200-R70 (with the RCA replacement ratio equal to 70%) are respectively 13.8% and 14.9% lower than that of the NACFSST column specimen D89-L1200-R0. For each specimen series, the experimentally obtained reduction factors for flexural buckling χ are plotted against the RCA replacement ratios r, as displayed in Fig. 11. It was observed that the reduction factors for flexural buckling χ are greater than 1.0 for the specimen series D101-L700, including three RACFSST and NACFSST column specimens with member relative slendernesses ranging from 0.38 to 0.40, revealing that the cross-section plastic resistances of the column specimens are marginally affected by flexural buckling in the relatively low range of member relative slendernesses. On the other hand, the flexural buckling reduction factors χ are less than 1.0 for the other three series of the RACFSST and NACFSST column specimens whose member relative slendernesses are greater than 0.43, indicating that the reductions in cross-section plastic resistances due to flexural buckling are now pronounced

Fig. 7. Experimental and numerical failure modes for typical specimen series D89-L1200.

in the intermediate and high range of member relative slendernesses and should be considered in the design. Moreover, as evident in Fig. 11 and Table 6, the reduction factors for flexural buckling of the RACFSST column specimens in each specimen series are approximately equal to that of the NACFSST column specimen, indicating that the reduction factor for flexural buckling is generally insensitive to the RCA replacement ratio.

2.5.3. Longitudinal strains of stainless steel tube

The distribution and development of the longitudinal strains at the mid-height of the stainless steel tubes of the circular RACFSST column specimens are studied in this section. Fig. 12 displays the load–longitudinal strain curves, measured by the three strain gauges (#1, #2 and #3 - see Fig. 6), for typical RACFSST column specimens D89-L700-R70 and D89-L1200-R70, while the longitudinal strains at the two extreme fibres (obtained from the strain gauges #1 and #3) and the mid-point of the extreme fibres (recorded from the strain gauge #2) of the stainless steel tubes at five different load levels – $0.2N_u$, $0.4N_u$, $0.6N_u$, $0.8N_u$ and N_u are collected and displayed in Fig. 13; note that negative and positive values signify compressive and tensile strains, respectively. As can be seen from Fig. 12, the measured load–longitudinal strain curves from the three strain gauges have rather small difference up to around $0.5N_u$–$0.6N_u$ (this is also evident in Fig. 13), revealing the insignificant effect of second-order bending moments at mid-height resulted from lateral deflections. When the applied compression load was increased from $0.6N_u$ to N_u, the discrepancy between the longitudinal strains at the three measured positions became increasingly large, owing to the rapid increase in lateral deflections and thus more pronounced influence of the resulting second-order bending moments. Then, in the post-ultimate loading phase, some parts of the mid-height cross-sections became even in tension, as reflected by the positive values of the longitudinal stains in Fig. 12; this is because the second-order bending moments generated from the mid-height lateral deflections were now more dominant than the compression loads.

3. Numerical modelling

3.1. General

Following the testing programme, a numerical modelling programme was conducted using the finite element (FE) software ABAQUS [30]. FE models were developed in Section 3.2, with the modelling procedures, assumptions and techniques described in detail. The developed FE models were then validated against the test results in Section 3.3. Finally, parametric studies were conducted by using the validated FE models to generate a numerical data bank over a wide range of cross-section dimensions and member effective lengths.

3.2. Development of FE models

Symmetry was exploited through modelling only half of the cross-section and half of the member effective length for each circular RACFSST or NACFSST column specimen. The eight-node brick element C3D8R [30] and four-node shell element S4R [30] were selected to model the RAC and NAC infill and stainless steel tubes, respectivley. A mesh sensitive study was carried out to seek suitable brick and shell element sizes that lead to both computational accuracy and efficiency. A series of element sizes varied between $D/5$ and $D/20$ were examined in the mesh sensitivity study and an identical size equal to $D/12$ was finally selected for both the brick and shell elements. The plastic material

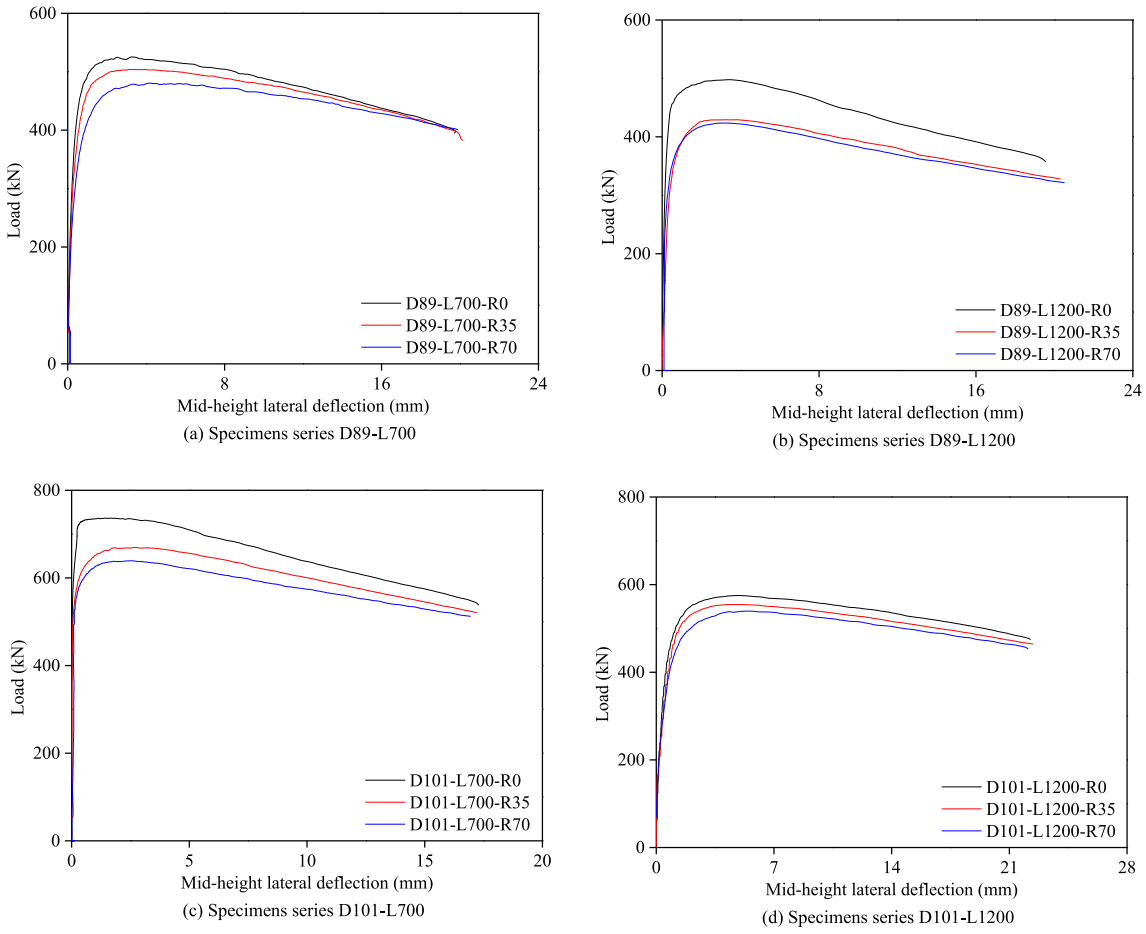

Fig. 8. Load—mid-height lateral deflection curves for four series of circular RACFSST and NACFSST column specimens.

model [29–34] was adopted for the material modelling of the stainless steel tubes. Specifically, for each tube size, the average measured (engineering) stress–strain curve was converted into the true stress–plastic strain curve and then assigned to the corresponding stainless steel tubes of the circular RACFSST and NACFSST column FE models. The concrete damage plasticity (CDP) model [29–34] was adopted for the material modelling of the RAC and NAC infill. In terms of the parameters relating to the material elastic behaviour, the elastic modulus for each type of concrete was taken as that measured from the cylinder tests and given in Table 1, while the Poisson's ratios of the three types of concrete were all taken as 0.2. The parameters relating to the material plastic behaviour, including the flow potential eccentricity, the dilation angle, the ratio of the compressive strength under biaxial loading to that under uniaxial loading and the ratio of the second stress invariant on the tensile meridian to that on the compressive meridian, were respectively taken as 0.1, 30°, 1.16 and 0.667, as recommended by Han et al. [35]. In order to consider the beneficial effect of the confinement from the outer stainless steel tube on the strength enhancement of the RAC or NAC infill, the equivalent uniaxial stress–strain (σ_c–ε_c) curves were determined from the confined concrete model developed by Han et al. [35], as given by Eqs. (6)–(10), in which $\xi_0 = \sigma_{0.2}A_s/f_cA_c$ is the confinement factor and β is a parameter proposed by Xiao et al. [36] to consider the influence of the RCA replacement ratio on the ultimate strain of RAC, and inputted into the CPD model. The tensile stress–strain relationship of each type of concrete was assumed to be linear elastic up to the ultimate tensile strength of $0.1f_c$, followed by an inelastic post-ultimate material response, characterised by means of fracture energy [37].

$$y = \begin{cases} 2x - x^2 & \text{for } x \le 1 \\ \dfrac{x}{\beta_o(x-1)^2 + x} & \text{for } x > 1 \end{cases} \tag{6}$$

$$y = \frac{\sigma_c}{f_c} \tag{7}$$

$$x = \frac{\varepsilon_c}{\beta\left(1300 + 12.5f_c + 800\xi_0^{0.2}\right) \times 10^{-6}} \tag{8}$$

$$\beta_o = \left(2.36 \times 10^{-5}\right)^{[0.25+(\xi_0-0.5)^7]} f_c^{0.5} \times 0.5 \ge 0.12 \tag{9}$$

$$\beta = 1 + \frac{r}{65.715r^2 - 109.43r + 48.989} \tag{10}$$

The surface-to-surface contact [29–34] was adopted to model the interaction between the stainless steel tubes and RAC and NAC infill. Specifically, a hard contact was used to represent the normal behaviour of the interaction, while a penalty method was adopted to simulate the tangential behaviour of the interaction, with the friction coefficient taken as 0.25 [31]. For the case of application of boundary conditions, the nodes of the end section of each circular RACFSST or NACFSST column FE model were coupled to a reference point located at the centre point of the end section, where the boundary conditions were then set; specifically, the reference point was fully restrained except for rotation about the axis of

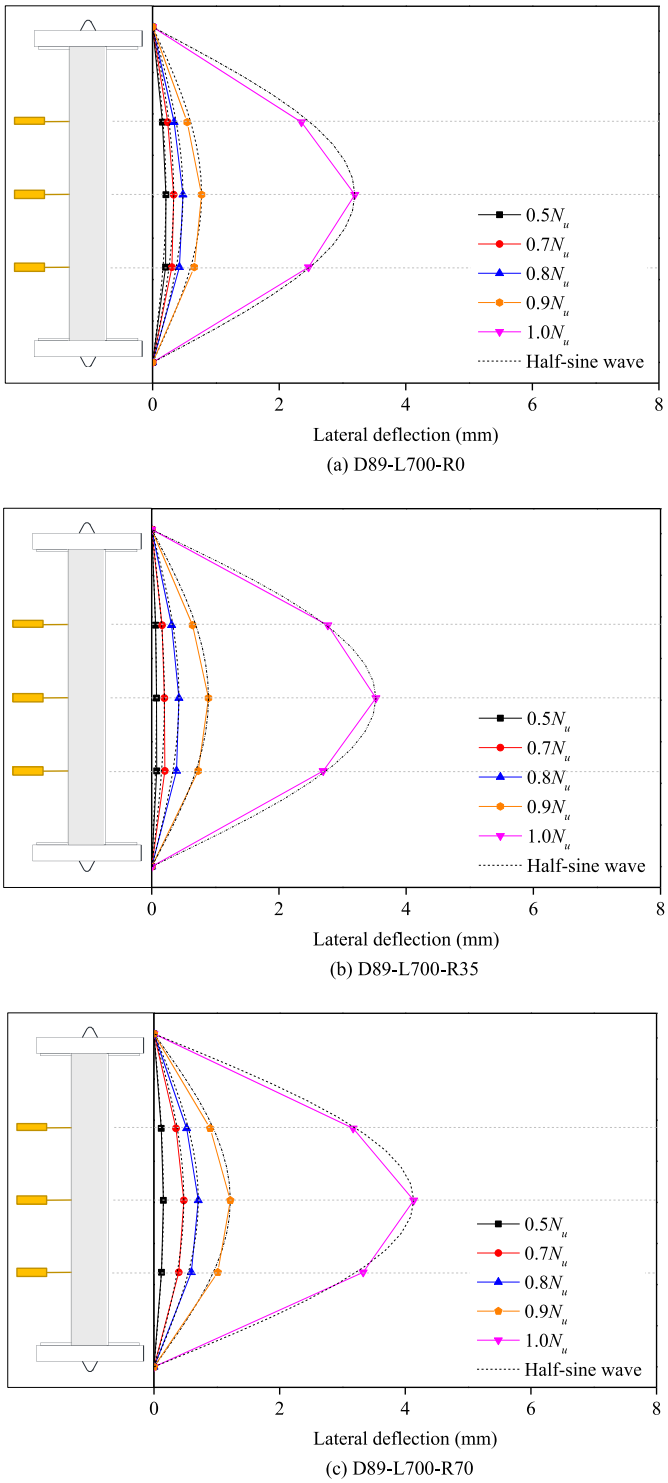

Fig. 9. Lateral deflection distributions for typical specimen series D89-L700.

buckling and longitudinal translation, to achieve the same pin-ended boundary conditions as those adopted in the tests.

The initial global geometric imperfections were incorporated into each circular RACFSST or NACFSST column FE model in the form of the lowest elastic global buckling mode shape. Three global imperfection magnitudes, including the measure overall global imperfection magnitude ($\omega_g + e_0$), $L_e/300$ and $L_e/1000$, were used to scale the initial global geometric imperfection distribution shape for each circular RACFSST or NACFSST column FE model, aiming at evaluating the influence of various global imperfection magnitudes on the numerical failure loads and seeking the most appropriate global imperfection magnitude to be adopted in the parametric studies. Finally, a static analysis [30], considering material and geometric nonlinearities, was carried out on each developed circular RACFSST or NACFSST column FE model, to obtain the

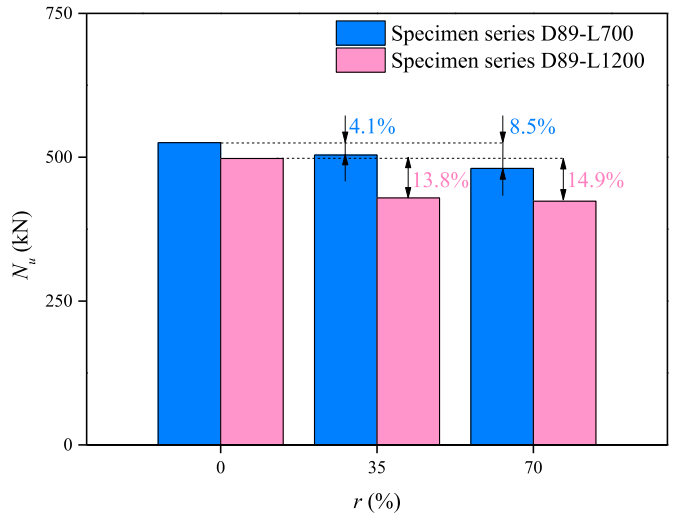

(a) Specimen series D89-L700 and D89-L1200

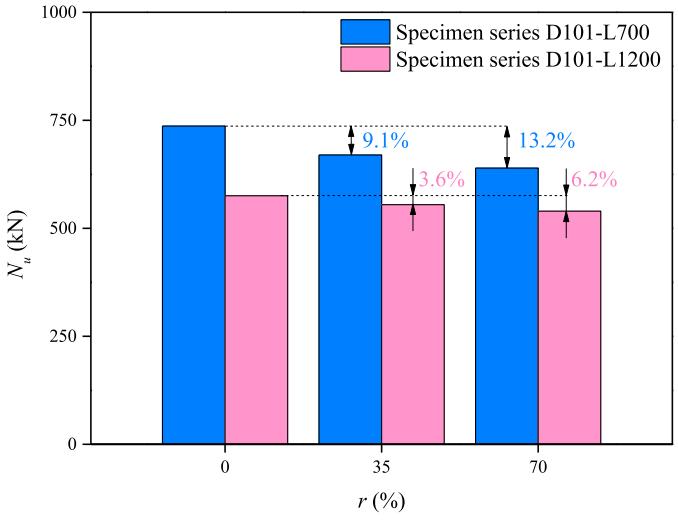

(b) Specimen series D101-L700 and D101-L1200

Fig. 10. Failure loads of four series of circular RACFSST and NACFSST column specimens.

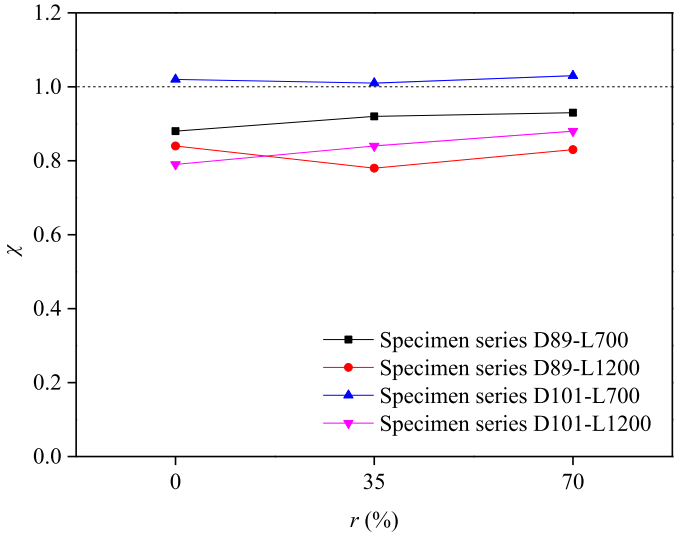

Fig. 11. Flexural buckling reduction factors for four series of circular RACFSST and NACFSST column specimens.

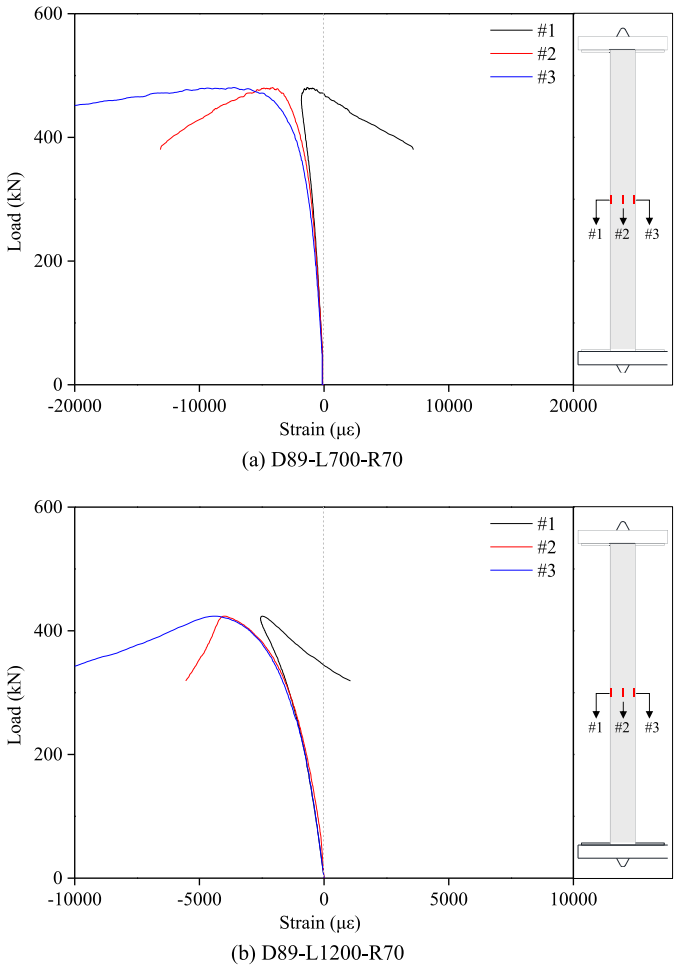

Fig. 12. Load–longitudinal strain curves for typical circular RACFSST column specimens D89-L700- R70 and D89-L1200-R70.

numerical failure load, load-mid-height lateral deflection curve and flexural buckling failure mode.

3.3. Validation of FE models

Validation of the developed circular RACFSST and NACFSST column FE models was conducted through comparisons of the obtained numerical results with the corresponding experimental observations. The ratios of the test to numerical failure loads for the twelve circular RACFSST and NACFSST column specimens are reported in Table 7. The results generally revealed that (i) the numerical failure loads were sensitive to the global geometric imperfection magnitudes, (ii) the adoption of the measured overall global geometric imperfection magnitudes led to the best agreement between the test and numerical failure loads, and (iii) accurate predictions of the test failure loads were also obtained when the global geometric imperfection magnitude was taken as L_e/1000. The experimental and numerical load-mid-height lateral deflection curves for a typical specimen series D101-L700 (including two RACFSST column specimens D101-L700-R35 and D101-L700-R70 and one NACFSST column specimen D101-L700-R0) are compared in Fig. 14, indicating good agreement. The flexural buckling failure modes obtained from numerical modelling are also in good agreement with those observed from tests, as illustrated in Fig. 7. Overall, the developed FE models were capable of replicating the test structural responses of the circular RACFSST and NACFSST column specimens and therefore deemed to be validated.

3.4. Parametric studies

On the basis of the validated FE models, parametric studies were conducted to generate a numerical data bank on circular RACFSST and NACFSST columns over a wide range of cross-section dimensions and member effective lengths. In the parametric studies, the average measured stress–strain curve of the stainless steel CHS 89 × 3 was used and the global geometric imperfection magnitudes were taken as L_e/1000. Table 8 reports the key geometric parameters of the circular RACFSST and NACFSST column FE models in the parametric studies. Specifically, the outer diameters of the modelled stainless steel circular hollow sections were kept at 100 mm and six wall thicknesses respectively equal to 1.54 mm, 1.72 mm, 1.96 mm, 2.27 mm, 2.70 mm and 3.33 mm were adopted, with the resulting outer diameter-to-thickness ratios varied between 30 and 65. For each modelled circular hollow section, eleven effective member lengths ranging from 500 mm to 5500 mm were selected. Then, regarding each modelled stainless steel CHS column, three types of concrete infill (i.e. R0, R35 and R70) were employed. Finally, a total of 198 numerical data on RACFSST and NACFSST columns were generated.

4. Evaluation of international design codes

4.1. General

Given that there have been no existing design codes for stainless steel–recycled aggregate concrete composite structures, the relevant

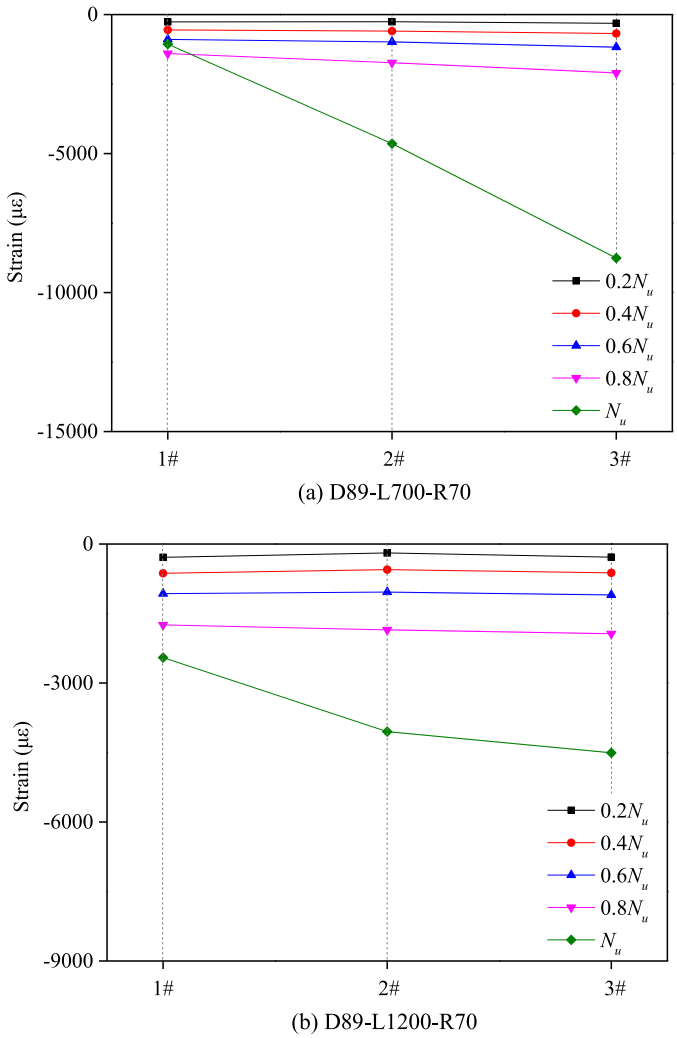

Fig. 13. Distributions of longitudinal strains for typical circular RACFSST column specimens D89- L700-R70 and D89-L1200-R70.

Table 7
Comparison of test failure loads with FE failure loads for various initial global geometric imperfection magnitudes.

Specimen	Test N_u/FE N_u		
	$\omega_g + e_0$	L_e/300	L_e/1000
D89-L700-R0	0.92	1.01	0.93
D89-L700-R35	0.95	1.04	0.96
D89-L700-R70	0.96	1.04	0.96
D89-L1200-R0	1.08	1.29	1.14
D89-L1200-R35	0.97	1.18	1.04
D89-L1200-R70	1.06	1.24	1.10
D101-L700-R0	1.00	1.13	1.05
D101-L700-R35	0.99	1.10	1.02
D101-L700-R70	1.01	1.11	1.03
D101-L1200-R0	0.98	1.11	0.99
D101-L1200-R35	1.03	1.16	1.04
D101-L1200-R70	1.07	1.20	1.08
Mean	1.00	1.13	1.03
COV	0.05	0.07	0.06

design rules for circular natural aggregate concrete-filled carbon steel tube (NACFCST) columns, as prescribed in EN 1994-1-1 [12], AS/NZS 5100 [13] and AISC 360–16 [14], were evaluated for their applicability to circular RACFSST and NACFSST columns. In each of the following sub-sections, the respective codified design rules for circular NACFCST columns were firstly presented, based on which the unfactored flexural buckling resistances of the considered circular RACFSST and NACFSST columns were calculated using the RAC and NAC material strengths and stainless steel 0.2% proof stresses. Quantitative evaluation of the applicability of each design code was then conducted by comparing the unfactored flexural buckling resistance predictions $N_{u,pred}$ against the test and numerical failure loads N_u, with the mean ratio of $N_u/N_{u,pred}$ and the corresponding coefficient of variation (COV) reported in Table 9.

4.2. European code EN 1994-1-1 (EC4)

The European code EN 1994-1-1 [12] specifies that the design flexural buckling resistance of a circular NACFCST column is determined as the product of the cross-section plastic resistance $N_{pl,Rd}$ and the reduction factor for flexural buckling χ_{EC4}, as given by Eq. (11). The cross-section plastic resistance $N_{pl,Rd}$ is calculated from Eq. (12); note that for circular NACFCST columns with member relative slendernesses less than or equal to 0.5, the interaction between the outer steel tubes and inner concretes may be taken into account through two coefficients η_c and η_a, as determined by Eqs. (13) and (14), respectively. EN 1994-1-1 [12] uses the same set of design buckling curves as that defined in EN 1993-1-1 [38] for calculating the reduction factor for flexural buckling χ_{EC4}, as given by Eq. (15), where ϕ is a buckling coefficient and

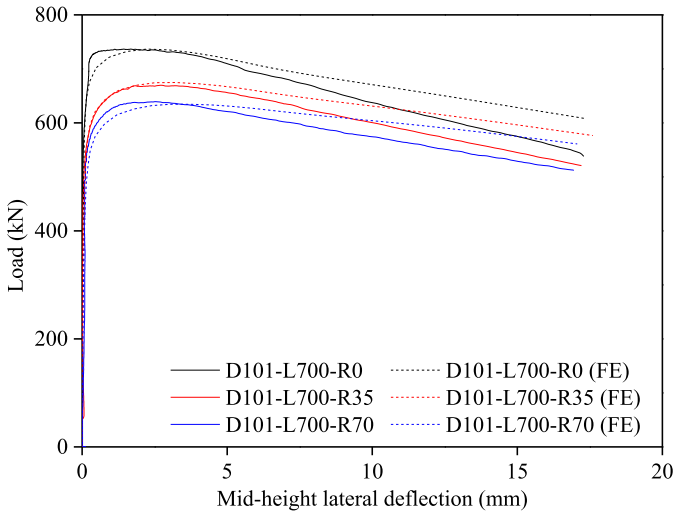

Fig. 14. Experimental and numerical load—mid-height lateral deflection curves for typical specimen series D101-L700.

Table 8
Key geometric parameters of circular RACFSST and NACFSST column FE models in parametric studies.

D (mm)	t (mm)	L_e (mm)
100	1.54	500, 1000, 1500, 2000, 2500, 3000, 3500, 4000, 4500, 5000, 5500
	1.72	500, 1000, 1500, 2000, 2500, 3000, 3500, 4000, 4500, 5000, 5500
	1.96	500, 1000, 1500, 2000, 2500, 3000, 3500, 4000, 4500, 5000, 5500
	2.27	500, 1000, 1500, 2000, 2500, 3000, 3500, 4000, 4500, 5000, 5500
	2.70	500, 1000, 1500, 2000, 2500, 3000, 3500, 4000, 4500, 5000, 5500
	3.33	500, 1000, 1500, 2000, 2500, 3000, 3500, 4000, 4500, 5000, 5500

Table 9
Comparisons of test and FE failure loads for circular RACFSST and NACFSST columns with codified flexural buckling resistance predictions.

Specimen type	Concrete type	No. of test data	No. of FE data	$N_u/N_{u,EC4}$		$N_u/N_{u,AS/NZS}$		$N_u/N_{u,AISC}$	
				Mean	COV	Mean	COV	Mean	COV
NACFSST	NAC (R0)	4	66	1.02	0.07	0.88	0.07	1.00	0.09
RACFSST	RAC (R35)	4	66	1.00	0.07	0.87	0.08	0.98	0.09
RACFSST	RAC (R70)	4	66	0.97	0.07	0.85	0.10	0.95	0.11
Total		12	198	1.00	0.07	0.86	0.09	0.97	0.10

determined from Eq. (16), where α is the imperfection factor, reflecting the effect of initial global geometric imperfections on the column buckling resistances and defined from the design buckling curves; for circular NACFCST columns with reinforcement ratios less than or equal to 3%, the design buckling curve 'a' is used, with α equal to 0.21.

$$N_{u,EC4} = \chi_{EC4} N_{pl,Rd} \tag{11}$$

$$N_{pl,Rd} = \begin{cases} A_s f_y + A_c f_c & \text{for } \bar{\lambda}_{EC4} > 0.5 \\ \eta_a A_s f_y + A_c f_c \left(1 + \eta_c \frac{t}{D} \frac{f_y}{f_c}\right) & \text{for } \bar{\lambda}_{EC4} \le 0.5 \end{cases} \tag{12}$$

$$\eta_c = 4.9 - 18.5\bar{\lambda}_{EC4} + 17\bar{\lambda}_{EC4}^2 \ge 0 \tag{13}$$

$$\eta_a = 0.25(3 + 2\bar{\lambda}_{EC4}) \le 1.0 \tag{14}$$

$$\chi_{EC4} = \frac{1}{\phi + \sqrt{\phi^2 - \bar{\lambda}_{EC4}^2}} \le 1 \tag{15}$$

$$\phi = 0.5\left[1 + \alpha(\bar{\lambda}_{EC4} - 0.2) + \bar{\lambda}_{EC4}^2\right] \tag{16}$$

For each considered circular RACFSST or NACFSST column, the EC4 flexural buckling resistance was determined by Eqs. (11)–(16). Table 9 reports the mean ratio of $N_u/N_{u,EC4}$ and the corresponding COV for each of the three types of composite columns (i.e. RACFSST columns with the RCA replacement ratios of 35% and 70% as well as NACFSST columns with the RCA replacement ratio of 0%), revealing that EN 1994-1-1 [12] yields a high level of design accuracy, on average. The test and numerical failure loads for the three types of circular RACFSST and NACFSST columns are normalised by the cross-section plastic resistances and plotted against the member relative slendernesses in Fig. 15, together with the EC4 design buckling curve defined by Eq. (15). The graphical comparison results revealed that (i) the three sets of normalised data points for circular RACFSST and NACFSST columns show little disparity and (ii) the EC4 design buckling curve can generally capture all the data points, but lies above those data points with member relative slendernesses between around 0.5 and 1.5 (i.e. leading to unsafe resistance predictions). Overall, it can be concluded that EN 1994-1-1 [12] leads to overall accurate flexural buckling resistance predictions when used for circular RACFSST and NACFSST columns, but some of the resistance predictions are unsafe for intermediate columns with member relative slendernesses between around 0.5 and 1.5.

4.3. Australian/New Zealand standard AS/NZS 5100 (AS/NZS)

The Australian/New Zealand standard AS/NZS 5100 [13] uses similar design rules to calculate the flexural buckling resistances of circular NACFCST columns as those given in the European code EN 1994-1-1 [12], but with different equations for determining the effective flexural stiffness and flexural buckling reduction factor. The effective flexural stiffness $(EI)_{eff,AS}$, as specified in AS/NZS 5100 [13], is given by Eq. (17), based on which the AS/NZS elastic critical normal force for flexural buckling $N_{cr,AS/NZS}$ and member relative slenderness $\bar{\lambda}_{AS}$ can be calculated and different from their EC4 counterparts. The AS/NZS flexural buckling reduction factor χ_{AS} is calculated from Eq. (18), where α_b is the appropriate section constant and equal to −0.5 for NACFCST members with reinforcement ratios less than or equal to 3%, while ξ, η and α_a

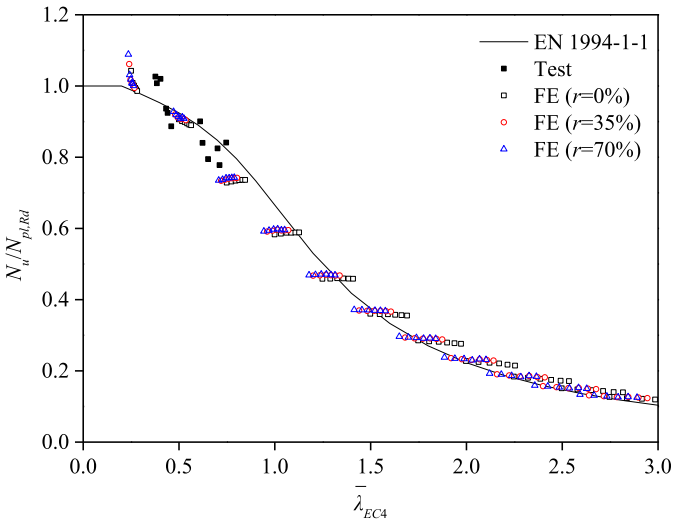

Fig. 15. Comparison of test and numerical failure loads with EC4 design buckling curve.

are the coefficients depending on the AS/NZS member relative slenderness, as defined by Eqs. (19)–(21), respectively.

$$(EI)_{eff,AS} = EI + E_{cm}I_c \tag{17}$$

$$\chi_{AS} = \xi\left[1-\sqrt{1-\left(\frac{90}{\xi(90\bar{\lambda}_{AS}+\alpha_a\alpha_b)}\right)^2}\right] \tag{18}$$

$$\xi = \frac{\left(\frac{90\bar{\lambda}_{AS}+\alpha_a\alpha_b}{90}\right)^2 + 1 + \eta}{2\left(\frac{90\bar{\lambda}_{AS}+\alpha_a\alpha_b}{90}\right)^2} \tag{19}$$

$$\eta = 0.00326(90\bar{\lambda}_{AS}+\alpha_a\alpha_b-13.5)\geq 0 \tag{20}$$

$$\alpha_a = \frac{2100(90\bar{\lambda}_{AS}-13.5)}{(90\bar{\lambda}_{AS})^2-15.3\times 90\bar{\lambda}_{AS}+2050} \tag{21}$$

The applicability of the AS/NZS design formulae to circular RACFSST and NACFSST columns was evaluated by comparing the flexural buckling resistance predictions against the test and numerical failure loads. The mean test and numerical to predicted failure load ratios $N_u/N_{u,AS/NZS}$ and the corresponding COVs for the three types of circular RACFSST and NACFSST columns are reported in Table 9. Fig. 16 depicts the normalised test and numerical failure loads, arranged by column type, together with the AS/NZS design buckling curve defined by Eq. (18). On the basis of the quantitative and graphical comparison results, it can be concluded that the AS/NZS design rules lead to unsafe flexural buckling resistance predictions over the whole considered range of member relative slendernesses up to 3.0 when used for circular RACFSST and NACFSST columns, indicating inapplicability.

4.4. American specification AISC 360–16 (AISC)

The compression resistance of a circular NACFCST column failing by flexural buckling $N_{u,AISC}$, as specified in the American specification AISC 360–16 [14], is equal to the cross-section compression resistance N_{no} multiplied by the flexural buckling reduction factor χ_{AISC}, as shown by Eq. (22). The AISC cross-section compression resistance N_{no} is determined from Eq. (23), while the AISC flexural buckling reduction factor is defined by Eq. (24), where $\bar{\lambda}_{AISC} = \sqrt{N_{no}/N_{cr}}$ is the AISC member relative slenderness, where the elastic critical normal force for flexural buckling N_{cr} is now calculated using Eq. (3), but with the AISC effective flexural stiffness $(EI)_{eff,AISC}$ given by Eq. (25) replacing $(EI)_{eff,EC4}$.

$$N_{u,AISC} = \chi_{AISC}N_{no} \tag{22}$$

$$N_{no} = f_yA_s + 0.95f_cA_c \tag{23}$$

$$\chi_{AISC} = \begin{cases} 0.658^{\bar{\lambda}^2_{AISC}} & \text{for } \bar{\lambda}^2_{AISC}\leq 2.25 \\ \dfrac{0.877}{\bar{\lambda}^2_{AISC}} & \text{for } \bar{\lambda}^2_{AISC}>2.25 \end{cases} \tag{24}$$

$$(EI)_{eff,AISC} = EI + \left[0.45 + 3\left(\frac{A_s}{A_s+A_c}\right)\right]E_{cm}I_c \tag{25}$$

The AISC design flexural buckling resistances for circular RACFSST and NACFSST columns were then calculated from Eqs. (22)–(25) and compared with the test and numerical failure loads. The mean $N_u/N_{u,AISC}$ ratio and the corresponding COV for each type of circular RACFSST and NACFSST columns are reported in Table 9, while comparisons of the AISC design buckling curve defined by Eq. (24) with the test and numerical failure loads are presented in Fig. 17. The quantitative and

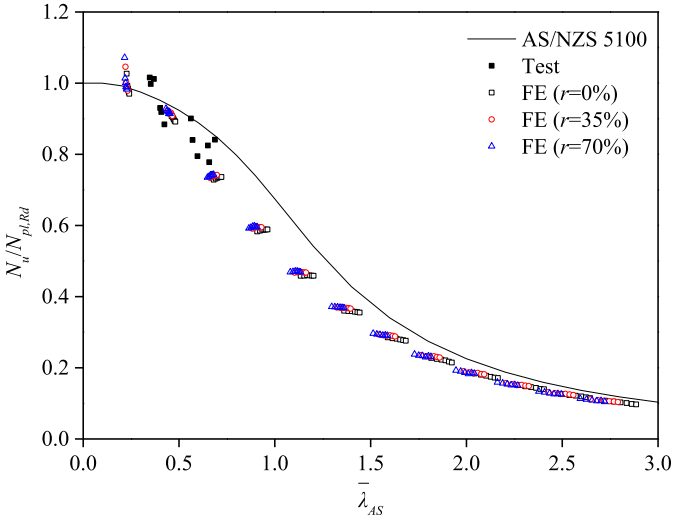

Fig. 16. Comparison of test and numerical failure loads with AS/NZS design buckling curve.

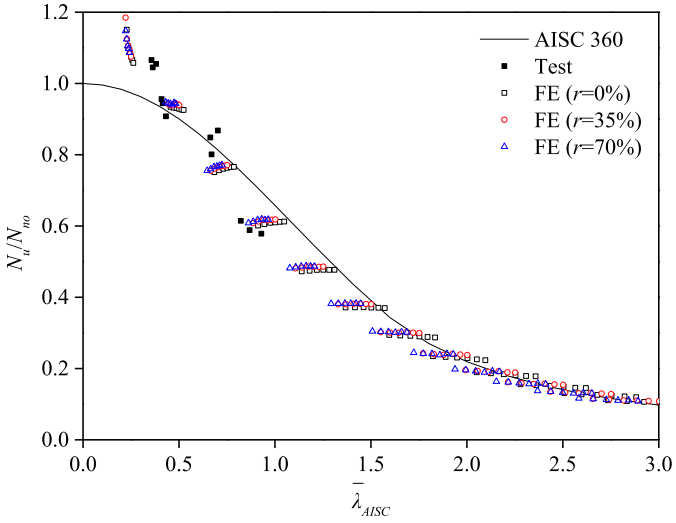

Fig. 17. Comparison of test and numerical results with AISC design buckling curve.

graphical comparison results demonstrated that the AISC design rules over-predict the flexural buckling resistances for all three types of circular RACFSST and NACFSST columns, though with an overall good level of design accuracy. In comparison with AS/NZS 5100 [13], AISC 360–16 [14] generally offers less over-predicted resistance predictions, but with a higher degree of scatter.

5. Conclusions

A comprehensive experimental and numerical modelling programme has been conducted to investigate the flexural buckling behaviour and resistances of circular RACFSST columns. The experimental programme comprised material tests, initial global geometric imperfection measurements and pin-ended column tests. The experimental results, including the failure loads, lateral deflections, load–deformation curves and failure modes, were fully reported and discussed. The development and distribution of the longitudinal strains of the outer stainless steel tubes were also analysed. The experimental programme was supplemented by a numerical modelling programme, in which FE models were firstly developed and validated against the test results and then used to conduct parametric studies for generating further numerical data on circular RACFSST columns over a wide range of cross-section dimensions and member lengths. Owing to the lack of existing design codes for recycled aggregate concrete–stainless steel composite structures, the corresponding design rules for circular NACFCST columns, as set out in EN 1994-1-1 [12], AS/NZS 5100 [13] and AISC 360 [14], were evaluated for their applicability to circular RACFSST columns, based on the obtained test and numerical data. The evaluation results generally indicated that (i) AS/NZS 5100 [13] results in unsafe flexural buckling resistance predictions over the whole considered range of member relative slendernesses when used for circular RACFSST columns, (ii) AISC 360 [14] yields an overall good level of design accuracy, but with many over-predicted resistances, and (iii) EN 1994-1-1 [12] offers the most accurate design flexural buckling resistances among the three design codes, though still with some unsafe resistance predictions for those intermediate columns with member relative slendernesses between around 0.5 and 1.5.

Declaration of Competing Interest

The authors declare that they have no known competing financial interests or personal relationships that could have appeared to influence the work reported in this paper.

Acknowledgements

The research work described in this paper was supported by Singapore Ministry of Education Academic Research Fund (AcRF) Tier 1 Grant (Project Number: RG95/18). The recycled coarse aggregates used in the present research were sponsored by Pan-United Corporation Ltd.

References

[1] Z. Chen, J. Xu, Y. Chen, E.M. Lui, Recycling and reuse of construction and demolition waste in concrete-filled steel tubes: a review, Constr. Build. Mater. 126 (2016) 641–660.
[2] Y.-F. Yang, L.-H. Han, Compressive and flexural behaviour of recycled aggregate concrete filled steel tubes (RACFST) under short-term loadings, Steel Compos. Struct. 6 (2006) 257–284.
[3] J. Xiao, Y. Huang, J. Yang, C. Zhang, Mechanical properties of confined recycled aggregate concrete under axial compression, Constr. Build. Mater. 26 (2012) 591–603.
[4] Y. Wang, J. Chen, Y. Geng, Testing and analysis of axially loaded normal-strength recycled aggregate concrete filled steel tubular stub columns, Eng. Struct. 86 (2015) 192–212.
[5] J. Chen, Y. Wang, C.W. Roeder, J. Ma, Behavior of normal-strength recycled aggregate concrete filled steel tubes under combined loading, Eng. Struct. 130 (2017) 23–40.
[6] Z. Liu, Y. Lu, S. Li, S. Yi, Behavior of steel tube columns filled with steel-fiber-reinforced self-stressing recycled aggregate concrete under axial compression, Thin-Walled Struct. 149 (2020).
[7] Y.-F. Yang, L.-H. Han, Experimental behaviour of recycled aggregate concrete filled steel tubular columns, J. Constr. Steel Res. 62 (2006) 1310–1324.
[8] Y.-C. Tang, L.-J. Li, W.-X. Feng, F. Liu, B. Liao, Seismic performance of recycled aggregate concrete–filled steel tube columns, J. Constr. Steel Res. 133 (2017) 112–124.
[9] Y.-C. Tang, L.-J. Li, W.-X. Feng, F. Liu, M. Zhu, Study of seismic behavior of recycled aggregate concrete-filled steel tubular columns, J. Constr. Steel Res. 148 (2018) 1–15.
[10] W. Li, Z. Luo, Z. Tao, W.H. Duan, S.P. Shah, Mechanical behavior of recycled aggregate concrete-filled steel tube stub columns after exposure to elevated temperatures, Constr. Build. Mater. 146 (2017) 571–581.
[11] Y.-F. Yang, G.-L. Ma, Experimental behaviour of recycled aggregate concrete filled stainless steel tube stub columns and beams, Thin-Walled Struct. 66 (2013) 62–75.
[12] EN 1994-1-1:2004, Eurocode 4: Design of Composite Steel and Concrete Structures – Part 1-1: General Rules and Rules for Buildings, European Committee for Standardization (CEN), Brussels, 2004.
[13] Australian/New Zealand Standards, Bridge design, Part 6: Steel and Composite Construction. AS/NZS 5100.6-2017, Sydney, Australia, 2017.
[14] American Institute of Steel Construction (AISC), Specification for Structural Steel Buildings. AISC 360-16, Chicago (IL), 2016.
[15] BS EN 1097-3, Tests for Mechanical and Physical Properties of Aggregates - Part 3: Determination of Loose Bulk Density and Voids, European Committee for Standardization (CEN), Brussels, 1998.
[16] BS EN 1097-6, Tests for Mechanical And Physical Properties of Aggregates - Part 6: Determination of Partical Density and Water Absorption, European Committee for Standardization (CEN), Brussels, 2013.
[17] BS EN 933-1, Tests for Geometrical Properties of Aggregates - Part 1: Determination of Particle Size Distribution - Sieving Method, European Committee for Standardization (CEN), Brussels, 1997.
[18] BS EN 12620, Aggregates for Concrete, European Committee for Standardization (CEN), Brussels, 2013.
[19] BS EN 12390-13:2013, Testing Hardened Concrete – Part 13: Determination of Secant Modulus of Elasticity in Compression, European Committee for Standardization (CEN), Brussels, 2013.
[20] EN ISO 6892-1, Metallic Materials – Tensile Testing – Part 1: Method of Test at Room Temperature, European Committee for Standardization (CEN), Brussels, 2009.
[21] W. Ramberg, W.R. Osgood, Description of Stress–Strain Curves by Three Parameters. Technical Note No. 902, National Advisory Committee for Aeronautics, Washington DC, 1943.
[22] H.N. Hill, Determination of Stress–Strain Relations from Offset Yield Strength Values. Technical Note No. 927, National Advisory Committee for Aeronautics, Washington DC, 1944.
[23] E. Mirambell, E. Real, On the calculation of deflections in structural stainless steel beams: an experimental and numerical investigation, J. Constr. Steel Res. 54 (2000) 109–133.
[24] K.J.R. Rasmussen, Full-range stress–strain curves for stainless steel alloys, J. Constr. Steel Res. 59 (2003) 47–61.
[25] L. Gardner, M. Ashraf, Structural design for non-linear metallic materials, Eng. Struct. 28 (2006) 926–934.
[26] I. Arrayago, E. Real, L. Gardner, Description of stress–strain curves for stainless steel alloys, Mater. Des. 87 (2015) 540–552.
[27] O. Zhao, L. Gardner, B. Young, Testing and numerical modelling of austenitic stainless steel CHS beam–columns, Eng. Struct. 111 (2016) 263–274.
[28] C. Buchanan, E. Real, L. Gardner, Testing, simulation and design of cold-formed stainless steel CHS columns, Thin-Walled Struct. 130 (2018) 297–312.
[29] A. He, Y. Liang, O. Zhao, Flexural buckling behaviour and resistances of circular high strength concrete-filled stainless steel tube columns, Eng. Struct. 219 (2020) 110893.
[30] ABAQUS, ABAQUS/Standard user's Manual Volumes I–III and ABAQUS CAE Manual. Version 6.12, Hibbitt, Karlsson & Sorensen, Inc, Pawtucket (USA), 2012.
[31] Z. Tao, B. Uy, F.-Y. Liao, L.-H. Han, Nonlinear analysis of concrete-filled square stainless steel stub columns under axial compression, J. Constr. Steel Res. 67 (2011) 1719–1732.
[32] Z. Tao, Z.-B. Wang, Q. Yu, Finite element modelling of concrete-filled steel stub columns under axial compression, J. Constr. Steel Res. 89 (2013) 121–131.
[33] W. Li, Y.-Z. Gu, L.-H. Han, X.-L. Zhao, R. Wang, M. Nassirnia, et al., Behaviour of ultra-high strength steel hollow tubes subjected to low velocity lateral impact: experiment and finite element analysis, Thin-Walled Struct. 134 (2019) 524–536.
[34] F. Wang, B. Young, L. Gardner, CFDST sections with square stainless steel outer tubes under axial compression: experimental investigation, numerical modelling and design, Eng. Struct. 207 (2020) 110189.
[35] L.-H. Han, G.-H. Yao, Z. Tao, Performance of concrete-filled thin-walled steel tubes under pure torsion, Thin-Walled Struct. 45 (2007) 24–36.
[36] J. Xiao, J. Li, C. Zhang, Mechanical properties of recycled aggregate concrete under uniaxial loading, Cem. Concr. Res. 35 (2005) 1187–1194.
[37] CEB-FIP (Euro-International Committee for Concrete (CEB)-International Federation for Prestressing (FIP)), Model Code for Concrete Structures. (CEB-FIP MC 2010), Thomas Telford, London, U.K., 2010
[38] EN 1993-1-1:2005+A1:2014, Eurocode 3: Design of Steel Structures – Part 1-1: General Rules and Rules for Buildings, European Committee for Standardization (CEN), Brussels, 2015.